Trivalent europium ions as a probe for the electric and magnetic local density of optical states in Si nanoresonators

Julia Attevelt

Supervisors: Jorik van de Groep MSc., and Prof. Dr. Albert Polman.

University of Amsterdam

Research project for the masters degree in Physics at the University of Amsterdam, the Netherlands, November 2013 - November 2014.

FOM Institute AMOLF

Center for Nanophotonics FOM Institute AMOLF Amsterdam, the Netherlands.

Abstract

Si nanoscale cylinders support strong geometrical resonances in the visible spectral range. These resonances are both magnetic and electric in nature. We study whether the magnetic $\lambda \sim 590\,\mathrm{nm}$ (MT) and electric $\lambda \sim 615\,\mathrm{nm}$ (ET) transitions of trivalent europium (Eu^{3+}) can be used as a probe to make a distinction between the magnetic and electric local density of optical states (LDOS) of the resonances. Si pillars are fabricated with diameters ranging from 125 nm to 275 nm, using electron beam lithography and reactive-ion etching. Finite-difference time-domain (FDTD) simulations and dark-field scattering spectroscopy are used to study the resonant modes. Coupling of the transitions to the optical resonators is studied by exciting Eu^{3+}-doped nanocrystals on top of the Si pillars, and detecting the photoluminescence of Eu^{3+}. From the relative intensities of the ET and MT luminescence we conclude that coupling does occur between $Eu^{3+}$and modes of the Si resonators. However, no proof is found that Eu^{3+} can discriminate between the magnetic or electric LDOS in Si resonators.

Contents

1 Introduction

The performance of many opto-electronic devices such as solar cells and optical sensors depends on the coupling and trapping of light at the surface of the device. Nanoscale particles that undergo resonant interactions with light can be used to enhance light-matter interactions at the surface, since they have large scattering cross sections at visible wavelengths. Plasmonic particles have proven to be useful in sensing/imaging [1], solar cells [2, 3] and light emitting diodes [4]. Such particles confine light through surface plasmons, which are collective oscillations of free electrons in metals. The performance of these particles is however limited by parasitic absorption in the metal.

Recent studies have shown that high index dielectric particles support geometrical resonances and also have the ability to strongly confine and scatter light [5, 6, 7]. The advantage of dielectric particles compared to plasmonic particles is that they are characterized by very low losses, since the resonances are displacement current distributions within the nanostructure. Spherical dielectric particles in a homogeneous medium are described in detail using Mie theory [8, 9, 10, 11].

Due to the high refractive index of Si, this is a good material to construct resonators. Si resonators have already shown great potential for applications (for instance on top of solar cells [12]). Si nanoparticles show electric dipole (ED) and magnetic dipole (MD) resonances in the visible and near infrared [13, 14, 15, 16]. The interplay between the ED and MD resonances allows for directional scattering of light [17, 18, 19], and a cylindrical particle shape allows for tuning the spectral spacing between the ED and MD resonances [6, 16, 19].

So far, the occurence of magnetic and electric modes of Si resonators has been studied using numerical simulations and angle resolved cathodoluminescence imaging spectroscopy [20]. Advances in the study of magnetic light-matter interactions provide a new tool for revealing information about the electrical and magnetic nature of the resonators. It has been shown that electric and magnetic dipole transitions (ET and MT) in trivalent europium (Eu^{3+}) can be used as a probe for the electric and magnetic local density of optical states (LDOS) [21]. The setup used in ref. [21] is similar to the setup used in the Drexhage experiment, in which it was demonstrated for the first time that the lifetime of atomic transitions changes due to the LDOS imposed by a reflective mirror [22].

Here, we investigate whether the ET and MT of trivalent europium (Eu^{3+}) can be used as a probe for the electric and magnetic LDOS in cylindrical Si resonators. We use the relative ratio of the ET and MT luminescence to study whether a particular ET or MT transition couples to the electric or magnetic LDOS of the resonator. When the ET couples more dominantly to the ED mode in the resonator and the MT transition to the MD mode, then Eu^{3+} can be used as a probe for those resonances in the Si resonator.

1.1 Research plan and Outline

The outline of the rest of this thesis is as follows: In Chapter 2 theory on dielectric resonators and trivalent europium is discussed as a background. The sample fabrication and characterization is described in chapter 3. Numerical simulations and dark-field scattering spectroscopy measurements to characterize the resonant modes of Si pillars are presented in Chapters 4 and 5, respectively. Chapter 6 reports on the photoluminescence experiments, performed with $LaPO_4$:Eu^{3+} nanocrystals, used to study the coupling between the emitters and resonant modes. Conclusions and an outlook are provided in Chapter 7.

2 Theory

2.1 Cylindrical Si nanoscale resonators

Resonances occuring in Si nanoscale particles are geometrical resonances similar to Mie-modes in spheres. Mie modes are named after the German physicist Gustav Mie (1869-1957), which are solutions of Maxwell's equations for a plane wave incident on a spherical particle in a homogeneous medium [10]. In this thesis we consider vertically oriented cylindrical Si particles with finite length. For such vertically oriented finite cylindrical particles no analytical solutions exist, and resonance spectra are calculated numerically.

To characterize the resonances, the normalized scattering cross section Q_{scat} can be used, which is defined as the particle scattering cross section divided by its geometrical cross section: $Q_{\text{scat}} = \sigma_{\text{scat}}/\sigma_{\text{geo}}$. For cylindrical Si resonators the scattering cross section at resonance is $5-10$ times larger than the geometrical cross section [12]. Consequently, a $10-20\%$ surface coverage with these nanostructures is enough for full interaction of the incoming radiation with the resonators.

Resonances occur when the incident wavelenght (λ) inside the particle is approximately equal to the particle diameter (d): $d \approx \lambda/n$, where n is the refractive index of the dielectric material. The Mie-like modes can have different modal behavior such as an electric dipole (ED), magnetic dipole (MD) or higher order modes. In Fig. 2.1, a schematic respresentation is shown of ED and MD modal field profiles in a dielectric cylinder. These resonances are driven by a horizontally polarized electromagnetic plane wave. The ED is characterized by an oscillating displacement current, parallel to the driving field polarization, inducing an oscillating electric dipole moment (red arrow $\vec{p}$ in left cylinder). For high index nanoparticles that induce sufficient retardation in the driving field while propagating through the nanoparticle, the displacement current can also give rise to an effective current loop (orange loop in the right dielectric cylinder). This happens when the polarization of the electric field is antiparallel at the opposite boundaries of the particle. This current loop induces a magnetic dipole moment (MD) perpendicular to the plane of the current loop [23, 15, 13].

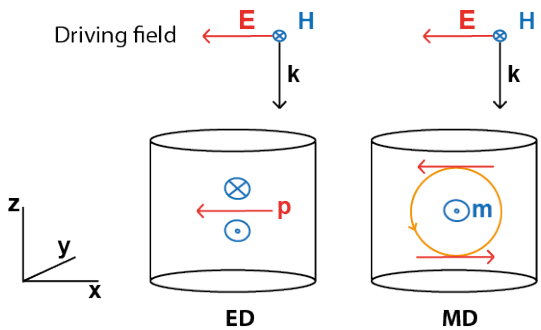

Figure 2.1: Schematic respresention of the electric and magnetic field in a dielectric nanoparticle at ED (left) and MD (right) resonance. The driving electromagnetic fields are polarized in the x-direction. The red arrows indicate the E-fields, and for the ED mode the orientation of the electric dipole moment $\vec{p}$. The blue circles indicate the magnetic fields. The orange circle in the MD mode indicates the displacement curent loop inducing a magnetic moment $\vec{m}$ in the y-direction.

2.2 Trivalent europium

Trivalent europium (Eu^{3+}) is one of the rare earth ions in the lanthanide series. In 1969, Dieke et al. investigated the energy levels of the lanthanides in several host crystals [24]. Nowadays, we see that emission of these ions is used in a range of technologies such as telecom fibers and fluorescent lighting.

The rare-earth ions are characterized by a partially filled $4f$ shell that is well shielded by $5s^2$ and $5p^6$ orbitals. In this shell both electric and magnetic dipole transitions can occur, which interact with the electric and magnetic component of electromagnetic waves, respectively [25]. In recent years the magnetic dipole transitions have attracted considerable attention [26, 27], because MD transitions could serve as active elements for nano-optics just as ED transitions have been used as local sources to control and study electric light-matter interactions [28, 29].

In Fig. 2.2, an emission spectrum of $LaPO_4$:Eu^{3+}nanocrystals dissolved in methanol (CH_3OH) is shown (a), along with their corresponding transition diagram (b). The $^5D_0$ is excited by a 395 nm pump wavelength using a Xenon lamp and a monochromator, and detected by a spectrometer. In this research, the magnetic dipole transition (MT) at $\sim$ 590 nm ($^5D_0 \rightarrow {}^7F_1$) and the electric dipole transtion (ET) at $\sim$ 615 nm ($^5D_0 \rightarrow {}^7F_2$) are used. Fig. 2.2a shows that the MT and ET luminescence intensities are of the same order of magnitude. Also, we observe that both decay channels share the same excited state ($^5D_0$). This means that both transitions have the same lifetime, which is determined by the transition with the highest decay rate. It is therefore only possible to distuinguish between states by the luminescence ratio of ET to MT transitions, not by lifetime measurements.

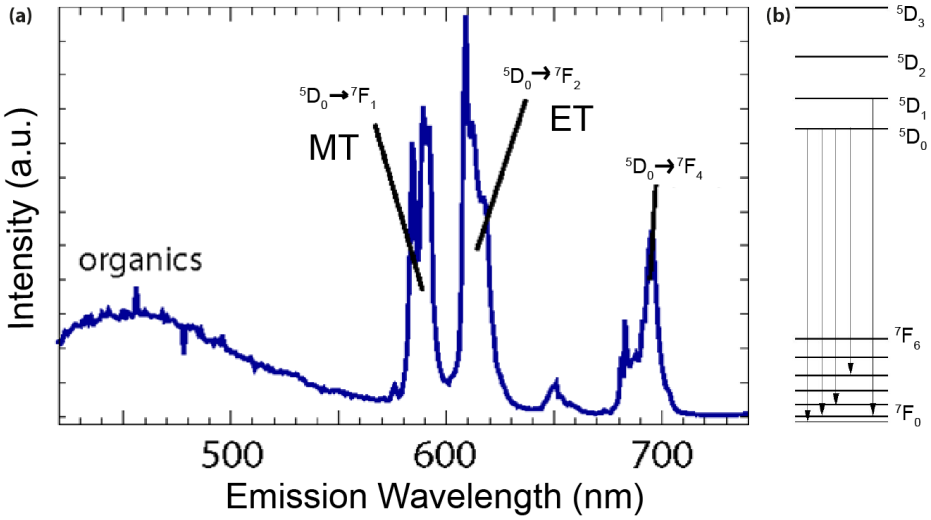

Figure 2.2: a) Emission spectra of intra-4f shell transitions of $LaPO_4$:Eu^{3+}nanocrystals (spectra obtained from ref. [30]). A magnetic dipole transition (MT) is present at $\lambda \sim 590\,\text{nm}$ and an electric dipole transition (ET) at $\lambda \sim 615\,\text{nm}$. b) Corresponding intra-4f shell transition diagram of Eu^{3+}.

3 Sample fabrication of cylindrical Si resonators

3.1 Design

To study the coupling between the MT ($\lambda \sim 590\,\text{nm}$) and ET ($\lambda \sim 615\,\text{nm}$) of Eu^{3+} and Mie modes, we construct Si pillars with ED and MD resonances around $\lambda \sim 600\,\text{nm}$. In ref. [6] it has been shown that 100 nm high Si pillars show a MD resonance at a diameter around 150 nm and ED resonance around a diameter of 220 nm. To systematically study the coupling, we therefore fabricated arrays of particles with diameters ranging from 100 nm to 250 nm with 5 nm step size. The total array size is $10\,\mu\text{m} \times 10\,\mu\text{m}$ and a pitch of 350 nm is used; the pitch size is large enough to fabricate the largest diameter particle array without nieghbouring particles touching, and small enough to avoid first order diffraction in free space. The particles are placed in an array to gain sufficient signal to noise in the measurements.

3.2 Fabrication methods

A $12\,\text{mm} \times 12\,\text{mm}$ chip of Si-on-insulator (SOI) wafer (100 nm Si device layer, 300 nm SiO_2 buried oxide layer, and a bulk layer of Si is baked for 5 min at 180 °C. The chip is spin coated with a thin hexamethyldisilazane (HMDS) adhesion layer (4000 rpm, 30 s). To evaporate the solvents, the HMDS layer is baked for 1 min at 180 °C. Hereafter, the sample is spin coated with a layer of negative tone resist (ma-N 2401, 2000 nm, 30 nm), and is baked for 1 min at 180 °C.

Using electron-beam lithography an etch mask is fabricated. This is done using a Raith e-LINE system with a 20 kV acceleration voltage and $7.5\,\mu\text{m}$ aperture, providing a beam current of 6 pA. The resulting dose is $310\,\mu\text{C/cm}^2$. The resist is developed by rinsing the sample in ma-D 332 S for 15 s, followed by a rinse in deionized H_2O to stop the development.

To anisotropically etch away the 100 nm thick Si layer around the mask, reactive ion etching (RIE) is used. For this, the sample is exposed to a gas mixture of CHF_3 (35 sccm) and SF_6 (5 sccm) for 3:30 min (forward power = 150 W). Residual resist is removed using a 10 min O_2 (20 sccm) plasma etch (50 W forward power).

3.3 Results

The fabricated sample is studied with an atomic force microscope (AFM) and a scanning electron microscope (SEM). In Fig. 3.1a, we see an AFM image of an array of particles with $d \sim 210\,\text{nm}$, from which we observe that the array is uniform over large areas. In Fig. 3.1b, a height profile measurement of three of these particles is presented, in which we observe that the height of the particles

is around 120 nm. This means we have etched $d \sim 20$ nm through the SiO_2 layer, since the Si layer is 100 nm. This has however no implications for the intended height of the Si pillar (100 nm), since these were protected by the etch mask.

In Fig. 3.2a, a SEM picture of a particle array is shown with $d \sim 175$ nm. We observe again a uniform array, and the cylinders clearly resemble the cylindrical shape. The pitch is measured to be 350 nm. However, we observe that cylinders are slightly tapered due to a non-perfect anisotropic etch. In Fig. 3.2b, a top view image of a particle can be seen, which allows for accurate measurement of the diameter. Measured diameters of the arrays range from around 125 nm to 275 nm.

Next, the arrays are inspected in an optical microscope using bright field illumination. The result is shown in Fig. 3.3. The second row of colored squares contains the 350 nm pitch arrays. Each square is a $10\,\mu$m $\times$ $10\,\mu$m array, with a fixed diameter. From left to right, the diameter increases from 125 nm to 275 nm. This increase in diameter is clearly visible; the transition from the blue tot red in the first half of the arrays indicates a redshift as expected for geometrical resonances. In the second half, a blue shift is observed, followed by another redshift. This is attributed to higher order resonances.

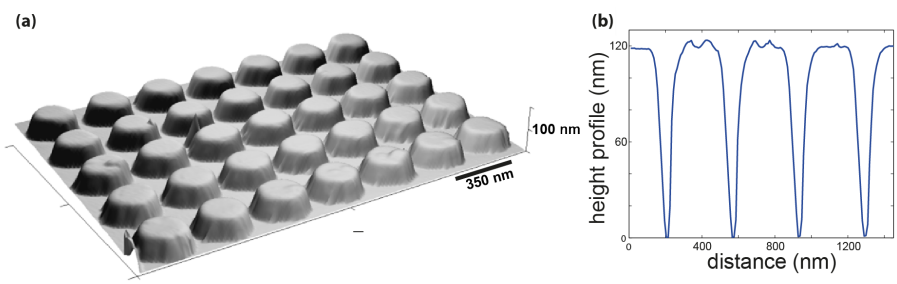

Figure 3.1: Atomic force microscopy (AFM) images. a) Overview of an array of particles b) Height profile measurement of three particles.

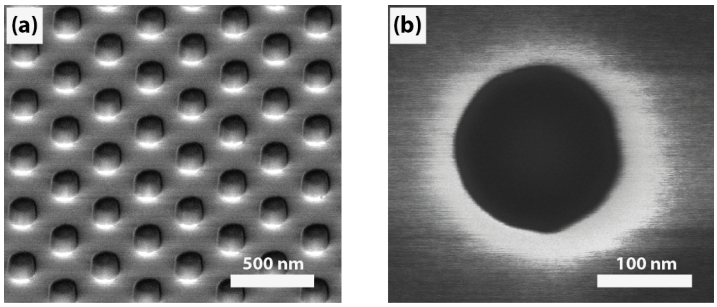

Figure 3.2: Scanning electron microscopy (SEM) images for a 120 nm high cylindrical Si particle array. a) Overview of array of particles (40° tilt), the pitch is 350 nm. b) Top view of one particle, the diameter is ~ 175 nm.

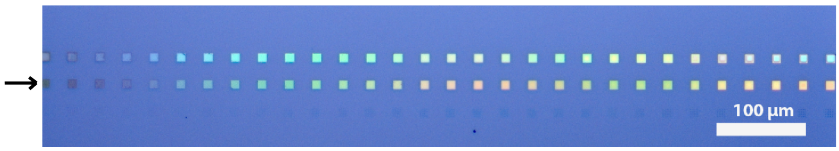

Figure 3.3: Bright field image overview of fabricated $10\,\mu$m $\times$ $10\,\mu$m Si particle arrays. Each square is one array. The row indicated by arrows is used for measurements. Each array contains particles with a 350 nm pitch and diameters range from around 125 nm on the left to 275 nm on the right.

4 FDTD simulations

Before we study how emitters couple to Si resonators, we first characterize the resonant properties of single and arrays of Si nanopillars. To this end we perform finite-difference time-domain (FDTD) simulations using the commercial software package Lumerical FDTD Solutions [31].

The resonances are studied by monitoring the normalized scattering cross section, defined as $Q_{\text{scat}} = \sigma_{\text{scat}}/\sigma_{\text{geo}}$ (scattering cross section normalized to geometrical cross section). To study the magnetic and electric nature of the resonances, modal field profiles inside the particles are investigated.

An overview of the simulation set ups is shown in Fig. 4.1. First, simulations are performed for a single Si particle in air with light incoming at normal incidence. Second, the effect of the SOI wafer substrate is investigated and the effect of arranging particles in an array is studied by setting periodic boundary conditions in this configuration. Furthermore, simulations are performed with plane waves incoming at off-normal incidence. This is studied because we will perform dark-field scattering measurements, in which light is incident from the sides.

In the FDTD simulations Q_{scat} is studied by using a total-field scattering-field source (TFSF) [31]. This is a broad band plane wave $\lambda = 450-750\,\text{nm}$ incoming at normal incidence, in which the light that has not been scattered is filtered out. To monitor the power of the scattered field, power monitors are placed around the TFSF source (Fig. 4.1a). Field monitors are positioned inside the particle to monitor the local field intensity in order to identify the corresponding current loops of ED and MD modes (Fig. 2.1). Perfectly matching layers (PML's) are placed on all sides of the simulation box in order to prevent reflections from the simulation boundaries. Finally, automatic non-uniform meshes are used and 5 nm mesh sizes. Optical constants for Si and SiO_2 are taken from Palik [32].

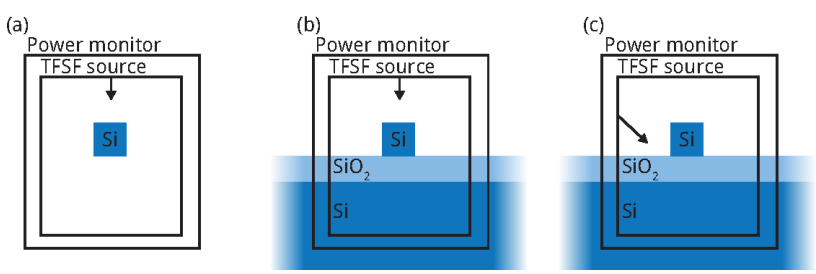

Figure 4.1: Simulation set ups for a) Single particle in air b) Single particles on substrate of SiO_2 and Si c) Plane waves incident at off-normal incidence.

4.1 Si particle in air

In this section, the resonant properties of cylindrical Si particles in air are investigated. Fig. 4.2a shows the spectral development of resonances as a function of diameter ($d = 100-300$nm) and wavelength ($\lambda = 450-750$nm). Also, the transition wavelenghts of the MT and ET of Eu^{3+}($\lambda \sim 590$ nm and $\lambda \sim 615$ nm) are indicated by the white horizontal lines. It can be observed that for $d = 100$ nm two modes occur at wavelenghts of 450 nm and 500 nm. The modes redshift for increasing diameter, and the peak Q_{scat} value stays roughly constant ($\sim$8). From $d > 160$ nm, the two modes gradually start to spectrally overlap, and support modes up untill $\lambda = 750$ nm at diameters around $d = 250$ nm. A higher order mode starts to occur for $d > 150$ nm.

The first two modes are of interest for answering the research question, because they clearly show resonances at the MT and ET wavelengths of Eu^{3+}. The first mode shows overlap with the transition wavelengths around $d = 160$ nm, and the second mode around $d = 200$ nm (white dashed lines in Fig. 4.2a). To take a closer look to these resonances we show the crosscuts of Q_{scat} for these particles diameters in Fig. 4.2b. We see again that the first two modes are separated spectrally for $d = 160$ nm (blue line), and show spectral overlap for $d = 200$ nm (red line).

To study the electric and magnetic nature of the resonances for the two particles, electric field profiles are extracted from the field monitors. The black dashed vertical lines in Fig. 4.2a indicate for which wavelenghts electric field intensities are shown ($\lambda = 600$ nm and $\lambda = 540$ nm for $d = 160$ nm, and $\lambda = 650$ nm and $\lambda = 600$ nm for $d = 200$ nm). The field profiles are presented in Fig. 4.3 where vertical crosscuts of the normalized electric field intensities and corresponding field lines (white lines) are shown. Comparing the schematic representation of magnetic and electric modes (see Figure 2.1) with the field profiles in Fig. 4.3, we see that field profiles of the lowest order modes (Fig. 4.3a and Fig. 4.3c) have electric field lines similar to the electric current loop in the MD schematic representation (orange). Therefore, we conclude that the lowest order mode is a MD mode. For the second mode (Fig. 4.3b and Fig. 4.3d) we see that the electric field lines match the schematic representation of an ED mode. In (Fig. 4.2a) we saw that the ED mode of the $d = 200$ nm nanopillars shows spectral overlap with the MD, which is observable in the field profiles as perturbations in the typical ED field lines (see Fig. 4.3d).

Combining the preceding observations, we conclude that two modes (a MD mode and ED mode) redshift with increasing particle diameter. This redshift develops more slowly for the MD mode than for the ED mode. As a result, for $d > 160$ nm, both resonances spectrally overlap. This shows that Si cylinders in air can be designed to match the ED and MD resonances to the MT and ET of Eu^{3+}emitters. However, the spectral overlap of the MD and ED mode for larger diameters prevents a clear independent coupling study of the ED mode and transitions of Eu^{3+}.

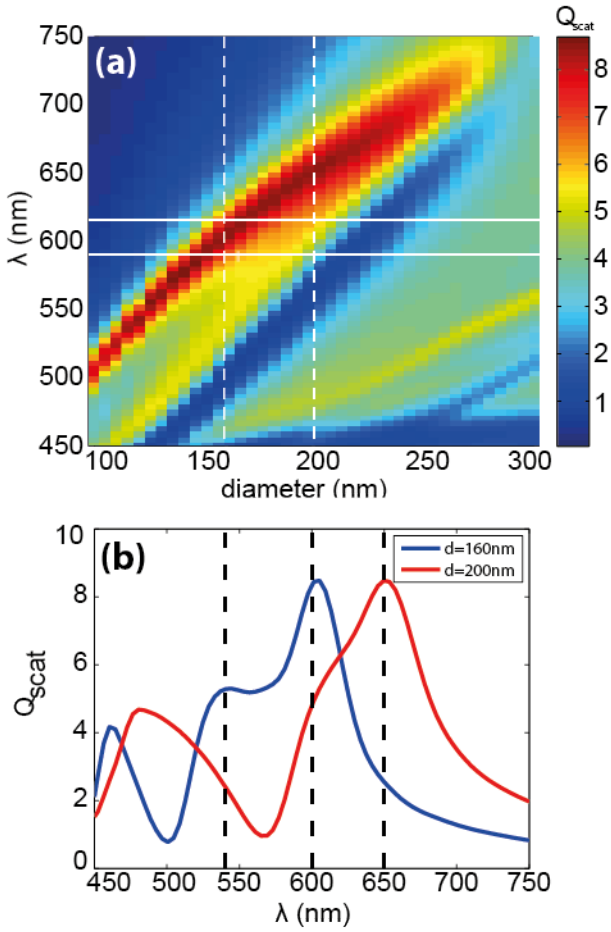

Figure 4.2: a) Q_{scat} (color) for 100 nm Si cylinders in air as function of wavelength and diameter. The two horizontal white lines show the MT and ET transition wavelengths of Eu^{3+}. The vertical white dashed lines correspond to crosscuts shown in b). b) Two Q_{scat} spectra at diameters of 160 nm (blue line) and 200 nm (red line) with MD and ED resonances around $\lambda = 600$ nm. The vertical black dashed lines correspond to the wavelengths for which the electric field intensity profiles are shown in Fig. 4.3.

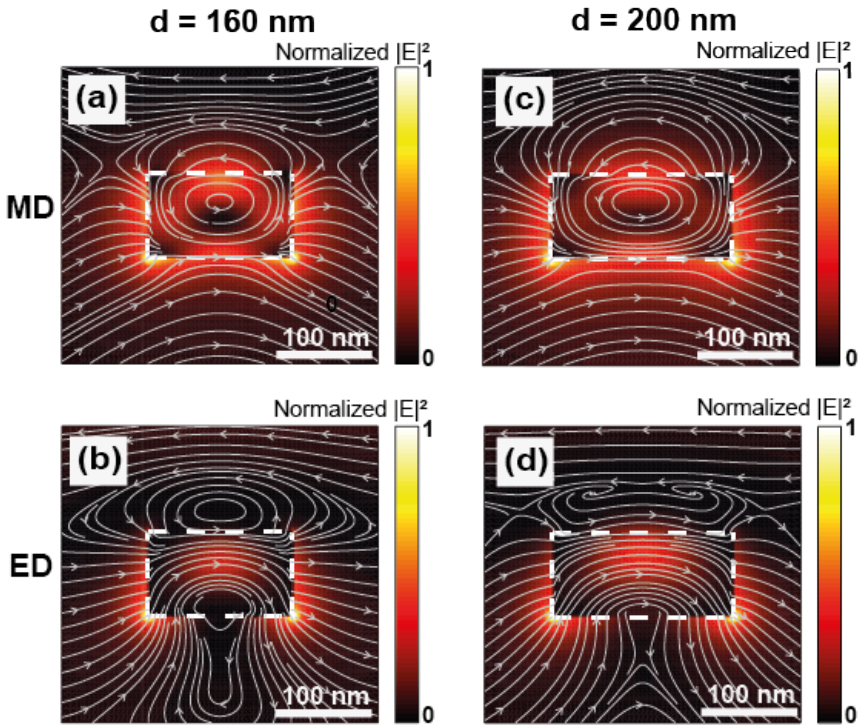

Figure 4.3: Vertical crosscuts through Si resonaters showing the normalized electric field intensity (color) and corresponding electric field lines (white). The two lowest order modes are shown for particles with $d = 160\,\text{nm}$ and $d = 200\,\text{nm}$. a) MD mode profile for $d = 160\,\text{nm}$ and $\lambda = 600\,\text{nm}$. b) ED mode profile for $d = 160\,\text{nm}$ and $\lambda = 530\,\text{nm}$. c) MD mode profile for $d = 200\,\text{nm}$ and $\lambda = 650\,\text{nm}$. d) ED mode profile for $d = 160\,\text{nm}$ and $\lambda = 600\,\text{nm}$.

4.1.1 Off-normal incidence

Here, Q_{scat} is studied while varying the angle of incidence (θ) of the plane wave. To do this, we rotate the particle in the simulation box. From three scattering spectra ($\theta = 0°, 50°, 90°$) in Fig. 4.4 we see that with increasing angle of incidence Q_{scat} resonance peaks become lower, and gradually MD and ED resonances spectrally separate (the ED mode blueshifts with increasing angle of incidence). This occurs since as the angle of incidence increases, the horizontal polarization of the driving field is alligned with the axis of the cylinder oriented, and thereby becomes more sensitive to particle height [6]. In this case the height is lower than the diameter ($h = 100\,\text{nm}$, $d = 200\,\text{nm}$), and therefore the resonance blueshifts for increasing angle of incidence. The MD mode occurs at the same wavelenght for the different angles, because the current loop inducing the MD mode (see Fig. 2.1) can be excited from the top and the sides. Thus,

using dark-field scattering measurements (Chapter 5), in which light is incoming at off-normal incidence, will result in larger spectral separation of the modes, which makes it easier to identify them.

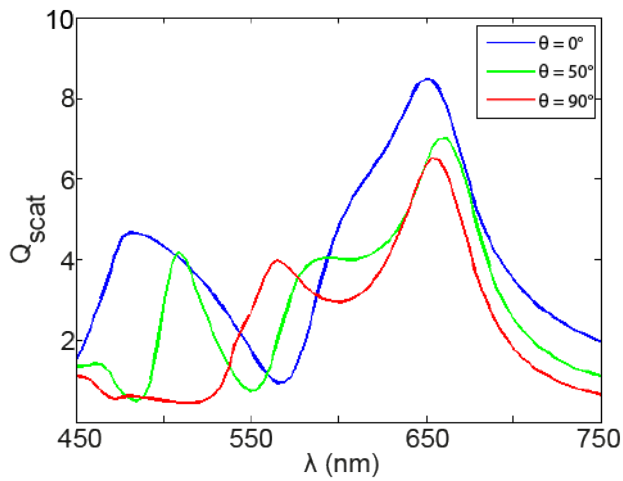

Figure 4.4: Scattering spectra Q_{scat} as function of angle of incidence for a Si particle in air. The particle diameter is 200 nm and incident wave angles θ are 0° (blue), 50° (green) and 90° (red).

4.2 Single Si particle on SOI substrate

To investigate the influence of the SOI substrate (which is used in the fabrication of the sample, see Section 3), a SiO_2 layer (300 nm) and a semi-infinite Si layer are added to the simulations (see Fig. 4.1b). Fig. 4.5a shows the spectral development of resonances as a function of diameter ($d = 100$–300 nm) and wavelength ($\lambda = 450$–750 nm), in which the white horizontal lines show the transition wavelenghts of the MT and ET of Eu^{3+}($\lambda \sim 590$ nm and $\lambda \sim 615$ nm, respectively). Crosscuts are indicated by the vertical white lines (at $d = 160$ nm and $d = 200$ nm) and shown in Fig. 4.5b.

Fig. 4.5a shows a mode shifting to the red from around $\lambda = 500$ nm at $d = 100$ nm to $\lambda = 750$ nm at $d = 250$ nm. The peak values of Q_{scat} range from $8-12$. This mode strongly overlaps with the MD mode of the single particle in air simulations (see Section 4.1), and from $d = 160$ nm the mode also shows overlap with the ED mode. Furthermore, compared to the single particle in air simulations, the ED mode is absent up until $d = 160$ nm, the mode profiles are broader, and peak values of Q_{scat} are higher.

Internal reflections at the $SiO_2$and Si interface gives rise to so called Fabry-Pérot resonances and could explain the absence and broadening of modes. To investigate this effect of internal reflection, simulations are performed for a particle

with $d = 160\,\text{nm}$ while varying the SiO_2 layer thickness. The results are shown in Fig. 4.6, in which we show Q_{scat} as function of wavelength ($\lambda = 450-750\,\text{nm}$) and thickness ($t = 100-500\,\text{nm}$). It can be observed that one mode is present from $t = 100$–180 nm. After this interval the mode splits into two modes between $t = 180-280\,\text{nm}$, in good correspondance with the MD and ED resonances of the single particle in air simulations (see Fig. 4.2b). This indicates that the single mode available in the first interval is a mix of an MD and ED resonance. Also, a higher order mode rises in the $t = 180-280\,\text{nm}$ interval in agreement with the single particle in air simulations. The trend of oscillation from one to three modes repeats itself while increasing the thickness of silica. This shows that the appearance of the number of modes depends on the thickness of the SiO_2 layer due to internal reflections. Since the available mode for the SOI substrate (where $t = 300\,\text{nm}$) is a mix of ED and MD, the desired coupling study is not possible for a single particle on SOI substrate.

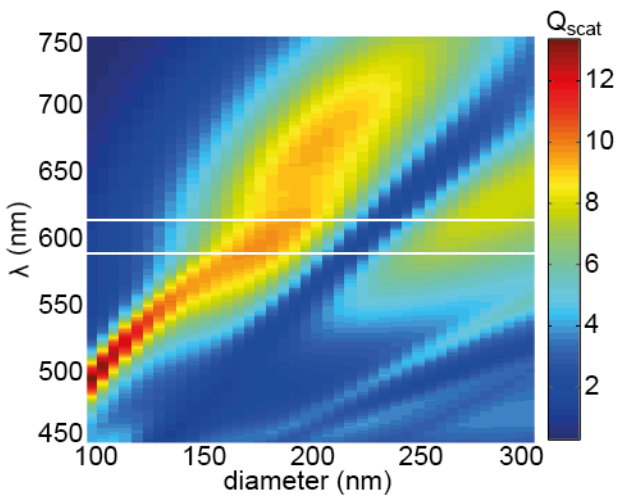

Figure 4.5: a) Q_{scat} for 100 nm Si pillars on a layer of SiO_2 (300 nm) and semi-infinite Si layer, as function of wavelength and diameter. The horizontal white lines to the MT and ET of Eu^{3+}.

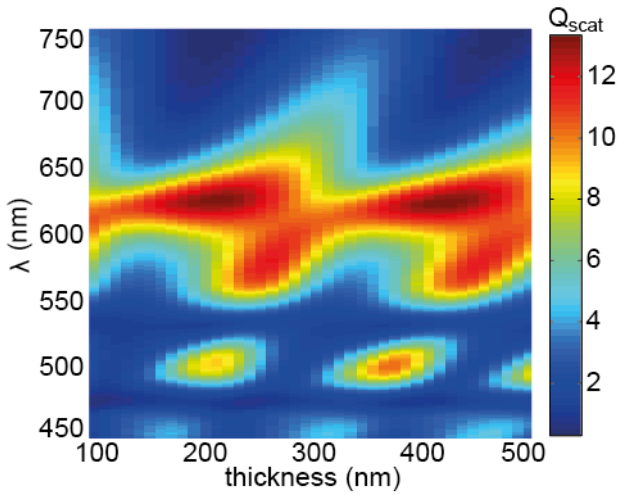

Figure 4.6: Spectra of Q_{scat} for a single particle with $d = 160\,\text{nm}$ as function of wavelength and thickness of the SiO_2 layer in the SOI substrate.

4.3 Particle array on substrate

The influence of arranging particles in an array with a pitch of 350 nm is investigated by setting 350 nm periodic boundary conditions in the simulations for a particle on SiO_2 and Si substrate (see Fig. 4.1b for the setup). The results are presented in Fig. 4.7, in which Q_{scat} is plotted as a function of diameter ($d = 100-300\,\text{nm}$) and wavelength ($\lambda = 450-750\,\text{nm}$). Comparing to the single particle simulations in air (Fig. 4.2), we observe again two spectrally separated MD and ED modes that gradually start to overlap spectrally. However, the peak values of resonances are higher ($Q_{\text{scat}} = 9-14$) and the resonances are sharper.

A possible explanation for the appearance of sharper and spectrally separated resonance peaks could be that by arranging particles in an array the radiative coupling occurs.

All above mentioned effects are benificial for the coupling studies, since a clear separation of MD and ED modes is desired. The Si cylinders arrays in air can be designed to match the ED and MD resonances to the MT and ET of Eu^{3+} emitters (white horizontal lines in Fig. 4.7). However, there is spectral overlap of the MD and ED mode where the ED starts to cross the MT and ET, so only a clear coupling study between the MD and MT can be performed.

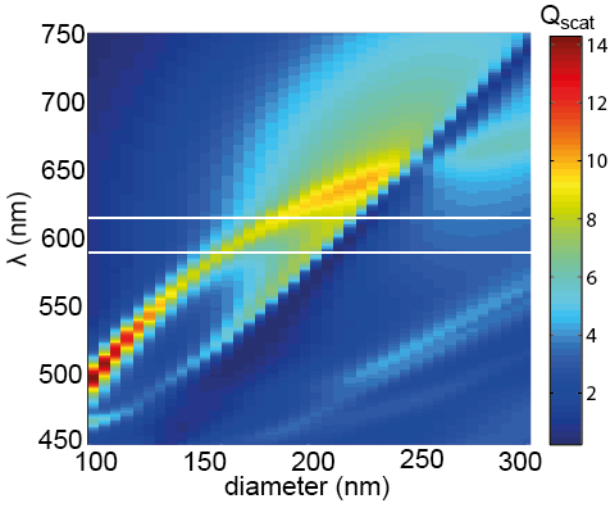

Figure 4.7: Q_{scat} (color) for 100 nm diameter Si pillars on a layer of SiO_2 (300 nm) and semi-infinite Si layer with 350 nm periodic boundary conditions as function of wavelength and diameter. The white horizontal lines correspond to the MT and ET of Eu^{3+}.

5 Dark-field scattering spectroscopy

Dark-field scattering spectroscopy is used to experimentally study resonance spectra in the fabricated particles. First, an overview is given of the experimental set-up. Thereafter, the results are presented and compared with the outcome of the FDTD simulations (from Chapter 4) .

5.1 Experimental setup

The dark-field spectroscopy setup is shown in Fig. 5.1a. A commercial Witec microscope system (model α300 SR) is used. The sample is illuminated with white light from a halogen lamp through a 50× dark-field objective (NA = 0.8). To correct for the system response, a spectrum is taken on a Lambertian isotropic scatterer and used as a reference, see (Fig. 5.1b). The range of angles that illuminate the sample is $65° - 75°$ (regardless of the azimuthal incident angle) and the scattered intensity is collected in reflection at angles $0-53°$. The collected light is coupled into a multi-mode detection fiber and sent to an Acton SP300i spectrometer, with a grating of 150 lines $mm^{-1}$and blaze wavelength of 500 nm. Light is detected with a CCD camera (1340 × 100 Si pixels). The spectra are the results of 25 accumulations of 500 ms and are accumulated 25×.

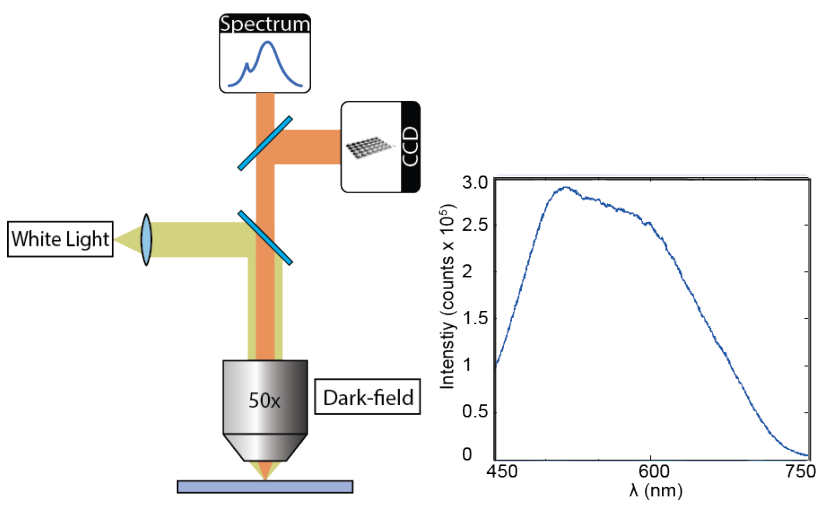

Figure 5.1: a) Experimental setup for dark-field scattering spectroscopy. b) Dark-field spectrum of lambertian isotropic scattering reference sample.

5.2 Results

Dark-field measurements are performed on all arrays of Si pillars with measured particle diameters ranging from 125 nm to 275 nm. In Fig. 5.2a the results of the

measurements are shown as a function of wavelength ($\lambda = 450-750\,\text{nm}$) and particle diameter ($d = 125-275\,\text{nm}$). Each measurement spectrum was devided by the Lambertian reference spectrum (see Fig. 5.1b), which is an isotropic scatterer with $R \sim 1$. The white horizontal lines show the MT ($\lambda \sim$590 nm) and ET ($\lambda \sim$615 nm) transition wavelengths of Eu^{3+}. The white vertical dashed lines indicate crosscuts at particle diameters of 160 nm and 200 nm, and are shown in Fig. 5.2b.

Several peaks can be observed between 475 nm and 625 nm, which redshift for increasing particle diameter, as expected for geometrical resonances. On the left side of the figure, the first mode starts to occur around a wavelength of 475 nm and a diameter of 130 nm. A second mode emerges at a diameter of 140 nm, and wavelength of 550 nm. From $d > 200\,\text{nm}$, these modes lose amplitude and new modes appear around $\lambda = 500\,\text{nm}$.

Comparing to the FDTD simulations (see Fig. 4.7), the spectral position of the first two modes shows good correspondance to the simulated spectra for the MD and ED modes respectively. Therefore, we attribute these measured peaks to the MD and ED mode. It is however surprising that modes in the measurements are not visible for $\lambda > 625\,\text{nm}$, for which the cause is unknown.

Based on the measured spectra, only the MD crosses the MT transition wavelength of Eu^{3+} of 595 nm for $d = 160-200\,\text{nm}$. For that reason we conclude that only the coupling with the MT and MD can be studied.

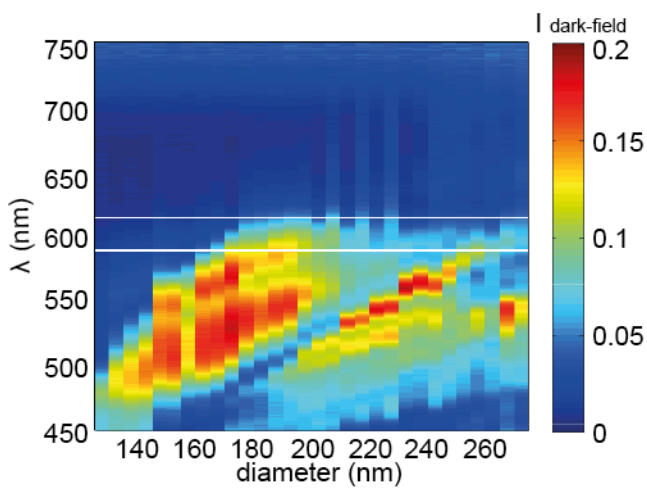

Figure 5.2: a) Dark-field scattering intensity (color) for arrays of Si pillars on a substrate of SiO_2 (300 nm) and a semi-infinite Si substrate, as function of wavelength and diameter. The white lines show the MT ($\lambda \sim 590\,\text{nm}$) and ET transition ($\lambda \sim 615\,\text{nm}$) wavelengths of Eu^{3+}.

6 Photoluminescence experiments of $LaPO_4$:Eu^{3+}nanocrystals

In order to investigate whether Eu^{3+} can be a probe for the magnetic and electric LDOS of Si resonators, we study the influence of the presence of resonators on the luminescence spectra of Eu^{3+}. Next, we analyze whether ED modes of Si resonators and the ET of Eu^{3+} couple preferentially to each other, as well as the MD and MT.

We dissolve $LaPO_4$:Eu^{3+} particles (of which synthesis procedure can be found in ref. [33]) in methanol and we dropcast the sample with a layer of this solution. Then, we excite the Eu^{3+} ions and detect luminescence spectra on each Si particle array.

When an MT ($\lambda \sim 590\,\mathrm{nm}$) or ET ($\lambda \sim 615\,\mathrm{nm}$) in Eu^{3+} couples to the resonant modes of the resonator, the LDOS increases. This results into an increased decay rate of the transition. Consequently, the luminescence intensity increases. Given the fact that the MT and ET are spectrally separated (see Section 2.2), the relative ratio of the ET and MT luminescence peak intensities varies if one of the two transitions is enhanced. This ratio can therefore be used to study whether a particular ET or MT transition couples to the electric or magnetic LDOS of the resonator.

To study the relative ratio, we define a branching ratio (B) as:

$$B = \frac{\max(I_{\mathrm{MT}})}{\max(I_{\mathrm{ET}})},$$

where $\max(I_{\mathrm{MT}})$ is the maximum intensity of the MT and $\max(I_{\mathrm{ET}})$ the maximum intensity of the ET. Mode coupling to the MT of Eu^{3+} results into a higher B, whereas coupling to the ET decreases B.

6.1 Experimental setup

The photoluminesence spectroscopy setup is shown in Fig. 6.1. To excite the Eu^{3+} ions, a 532 nm Yttrium Aluminium Garnet (YAG) pulsed laser (7-9 ps pulse width, 10 MHz repetition rate) is used. The laser beam is focussed on the sample with a 100× objective (Nikon CFI Plan Fluor, NA0.9). The laser spot has roughly a diameter of 10μm, which is a similar size as the particle array. The same objective collects the luminescence and sends it to a spectrometer (SpectraPro 2300i), and hereafter to a thermoelectrically cooled back-illuminated Si CCD array detector (Princeton Instruments PIXIS:100B). The integration time for the spectra is 1s.

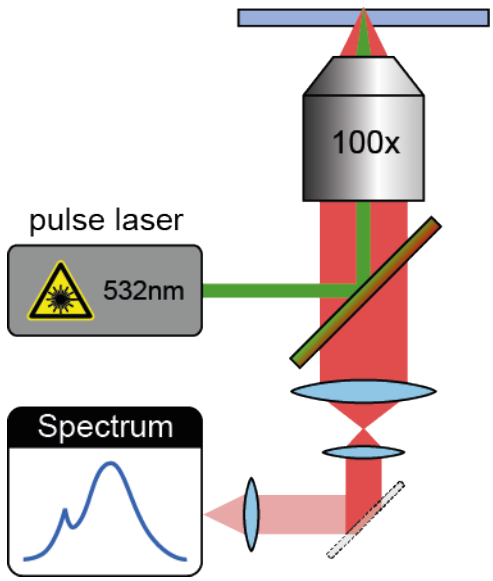

Figure 6.1: Experimental setup for photoluminescence experiments on Eu^{3+} ions.

6.2 Results

For each array photoluminescence spectra are measured. A typical spectrum is shown in Fig. 6.2. We observe the MT at $\lambda \sim 595$ nm and the ET at $\lambda \sim 615$ nm (labeled accordingly). Also, peaks can be observed around 650 nm, 685 nm and 700 nm. The spectra are in agreement with the spectrum for Eu^{3+} presented in Fig. 2.2.

For each array, the branching ratio (B) is calculated using the peak values of the MT and ET luminescence. In case of no coupling to Si resonators $B \approx 0.49$, which is calculated using a reference specrum taken next to the particle arrays on the sample. In Fig. 6.3a the branching ratio for all arrays is presented as function of the measured diameter of the Si resonators ($d = 125-275$ nm).

The branching ratio ranges from 0.44 to 0.57, and is centered around 0.49 (dashed horizontal line). For the smallest cylinders $d < 160$ nm (up to the first blue vertical line), the branching ratio fluctuates around 0.49. Thereafter, a decaying trend is observed, up until $d = 230$ nm (the second blue line). For $d > 230$ nm, an increasing trend is observed, raising B above the background level of 0.49. These modulations around the background value indicate that there is coupling between the transitions of $Eu^{3+}$and the LDOS of the Si resonators. The decrease in B ($d = 160-230$ nm indicates increased coupling to the ET transition, and the increase ($d > 230$ nm) stronger coupling to the MT transition. Given that the provided branching ratio is based on one measurement on each array, no estimation of errors is provided. Despite this, a clear

decaying and increasing trend compared to the background level is observable.

In Fig. 6.3b spectra of the dark-field scattering spectroscopy measurements are repeated for comparison (see Chapter 5). The branching ratio modulation ranges are shown by the vertical white lines (the same diameters as the blue lines in the branching ratio plot, see Fig. 6.3a)). Up until the first vertical line ($d < 160\,\text{nm}$) B fluctuates around 0.49, and therefore no mode coupling is present. This is supported by the fact that in this range the observed modes in the dark-field spectra are far away from the transitions wavelengths of Eu^{3+}. For $160 < d < 230\,\text{nm}$, the value of B indicates that coupling to the ET occurs. In the dark-field spectra a MD mode around 600 nm starts to rise in this region. For this mode the branching ratio is decaying and therefore the magnetic mode couples more strongly to the ET of Eu^{3+}. After the second white line (at $d = 230\,\text{nm}$) higher order modes arise. In this interval, the branching ratio increases, due to coupling to the MT of Eu^{3+}.

Based on the modulations of B, we can conclude that coupling with resonant modes around these transition wavelengths occurs. The modulations can be explained by coupling between the MD and ET, as well as between higher order modes and the MT. However, with the provided results no proof is found that Eu^{3+} transitions can be used as a probe to distinguish the magnetic and electric LDOS.

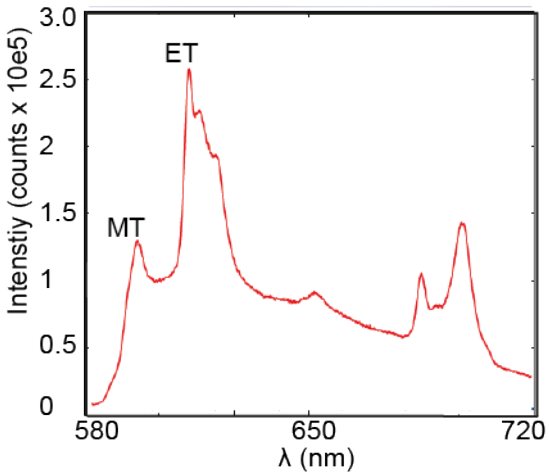

Figure 6.2: Luminescence of $LaPO_4$:Eu^{3+}detected for an array with Si resonators around $d = 175\,\text{nm}$, in which the MT and ET of Eu^{3+} are indicated.

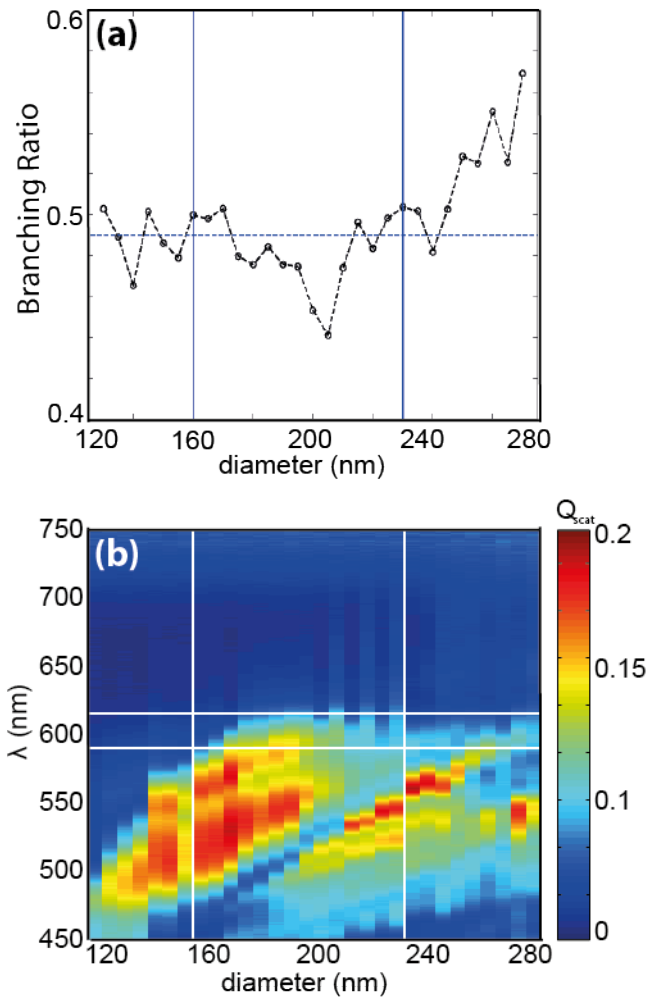

Figure 6.3: a) The measured branching ratio $B = \frac{\max(I_{\mathrm{MT}})}{\max(I_{\mathrm{ET}})}$ for Si resonator arrays with $d = 125\,\mathrm{nm} - 275\,\mathrm{nm}$. b) Dark field spectra of Si resonator arrays with $d = 125\,\mathrm{nm} - 275\,\mathrm{nm}$. Before the first vertical white line the branching ratio is constant around $B \approx 0.49$, after which the branching ratio decreases, and from the second white line the branching ratio increases.

7 Conclusion and Outlook

In this thesis we studied whether the MT ($\lambda \sim 595\,\text{nm}$) and ET ($\lambda \sim 615\,\text{nm}$) transitions of Eu^{3+} can be used as a probe for the electric and magnetic LDOS in dielectric resonators. We fabricated a sample of Si resonators coated with Eu^{3+}-doped nanocrystals. FDTD simulations showed that only the coupling of the MD mode in Si resonators and transitions of Eu^{3+} can be analyzed. The dark-field scattering spectroscopy measurements revealed experimental confirmation of the predicted MD and ED modes in the scattering spectra. Based on the provided dark-field spectra and FDTD simulations, we conclude that a coupling study is only possible between the MD and MT.

Our photoluminescence coupling experiments have shown that the resonant modes of Si pillars around 600 nm couple to MT and ET transitions of Eu^{3+}. Coupling is observed between the MD and ET, as well as between higher order modes and the MT. No evidence was found for Eu^{3+} as a probe to discriminate between the magnetic and electric LDOS in Si resonators, since MD modes of the resonators would then couple more strongly to the MT of Eu^{3+} than to its ET (see Chapter 1).

Future work will focus on searching for a measurement setup in which modes in the resonators above $\lambda = 625\,\text{nm}$ can be seen as well (for characterizing the Si pillars even better). Also, the homogeneity of the nanocrystal layer can be improved, for example by solving the crystals into Polymethyl Methacrylate (PMMA) as in ref. [34]. Another possibility is to construct a sample where Eu^{3+} is located inside the resonators. This is more ideal, because coupling can occur at the maximum of the field intensities. This is however not possible for Si resonators and Eu^{3+}, since the transitions of Eu^{3+} quench into the band gap of Si. For another dielectric material TiO_2, which has a higher band gap, this is a possibility. We have performed some first steps in fabricating a sample with TiO_2:Eu^{3+} resonators, of which the details can be found in the appendix (see Section 7).

Alltogether, this work is a guideline of the fabrication and characterization of arrays of Si pillars that can be used for studying the coupling between their resonant modes and transitions of Eu^{3+} ions. Furthermore, it has provided first results in answering whether Eu^{3+} ions can act as a probe and discriminate between the magnetic and electric LDOS in Mie resonators.

Appendix

Fabrication of TiO_2:Eu^{3+}

Here, an overview is given of fabricating a 250 nm layer of TiO_2:Eu^{3+} on a substrate of SiO_2 (quartz), with the peak concentration of Eu^{3+} in the middle of the TiO_2 layer. The first step in the fabrication is to evaporate a 250 nm layer of TiO_2 on a quartz substrate. This is done by e-beam evaporation. Europium was implanted into TiO_2, using ion beam implantation (performed at the Ion beam Centre at the university of Surrey). We aimed for a 1/10 atomic percentage as a peak concentration in the middle of the TiO_2 layer. For this a dose of 1.3535×10^{16} atoms/cm^2 and beam energy of 525 kV is required, which has been calculated using the commercial software package SRIM [35]. Elemental analysis has been performed with Energy-dispersive X-ray (EdX) spectroscopy of which the results are shown in Fig. 7.1. We see the expected characteristic X-ray peaks of Si, Ti, O and Eu and an indication of their concentration. Surprisingly, Ta is present as well. We attribute this to the Ta holder in which TiO_2 was kept in the evaporation process and herefore Ta has been evaporated together with TiO_2.

In order to search for an optimal activation temperature of Eu^{3+}, the intention was to search for the optimal photoluminescence signal for several sample annealed on different temperatures, $T = 800°, 900°$ and $1000°$ under vacuum for 30 min using a tube oven. However, we have tried to excite the TiO_2:Eu^{3+} in the same setup as for the coupling studies (see Section 6.1) and no photoluminescence at the MT and ET wavelenghts has been detected.

To test in another way whether the sample shows luminescence of Eu^{3+}, we have performed cathodoluminescence (CL) spectroscopy, since CL provides a broad band energy excitation source for which the excitation of Eu^{3+} ions efficiency is high. We have used the CL system at AMOLF (a description is given in [20]), with a 5 keV beam accelaration and 5 nA beam current. The results are shown in Fig. 7.2 for a TiO_2:Eu^{3+} sample annealed at $T = 900°$ (a) and a reference sample containing $LaPO_4$:Eu^{3+}(b). An ET transition ($\lambda \sim 615$ nm) is observable for the TiO_2:Eu^{3+} sample, and both an MT ($\lambda \sim 595$ nm) and ET for the reference sample. This shows that photoluminescence of Eu^{3+} for the ET of TiO_2:Eu^{3+} can be found. We also observe a strong luminescence increase for $\lambda < 600$ nm in the intensity profile of the TiO_2:Eu^{3+}sample (Fig. 7.2a), which is due to defect luminescence of the quartz substrate and embedded medium TiO_2. Since this increased luminescence is located at the MT wavelength of Eu^{3+}, we can not conclude if a MT of Eu^{3+} is available in the TiO_2:Eu^{3+} layer.

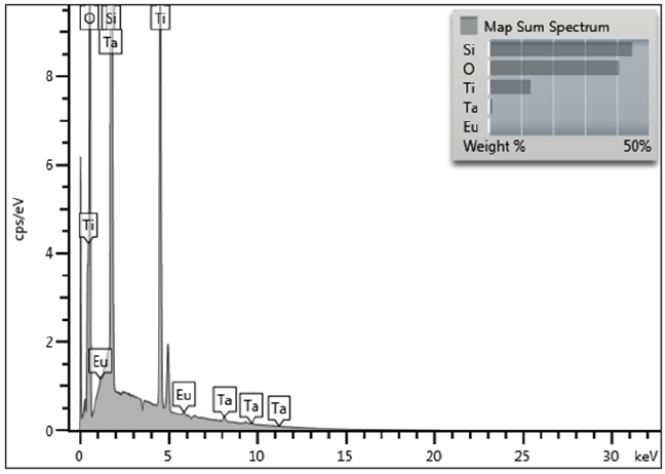

Figure 7.1: Elemental analysis of a SiO_2 substrate containing a 250 nm TiO_2:Eu^{3+} layer, using Energy-dispersive X-ray spectroscopy. Also a rough estimation of the atomic concentration (%) is shown in the right corner.

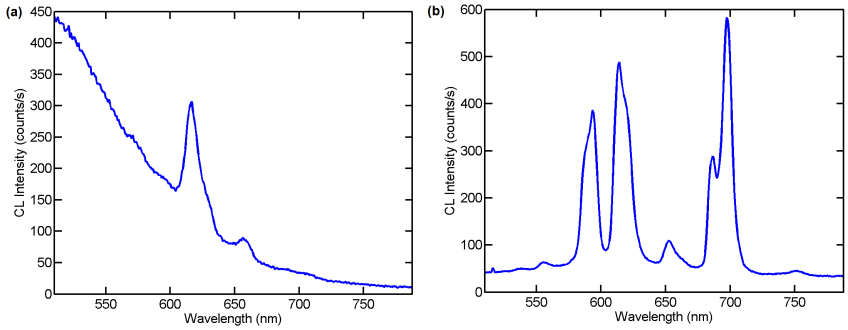

Figure 7.2: CL spectra as funcion of wavelength: a) TiO_2:Eu^{3+} sample annealed at T = 900°. b) a reference sample containing $LaPO_4$:Eu^{3+}.

References

[1] Christiane Hoppener and Lukas Novotny. Antenna-based optical imaging of single ca^{2+} transmembrane proteins in liquids. *Nano letters*, 8(2):642–646, 2008.

[2] Vivian E Ferry, Marc A Verschuuren, Hongbo BT Li, Ewold Verhagen, Robert J Walters, Ruud EI Schropp, Harry A Atwater, and Albert Polman. Light trapping in ultrathin plasmonic solar cells. *Optics Express*, 18(102):A237–A245, 2010.

[3] Harry A Atwater and Albert Polman. Plasmonics for improved photovoltaic devices. *Nature materials*, 9(3):205–213, 2010.

[4] Min-Ki Kwon, Ja-Yeon Kim, Baek-Hyun Kim, Il-Kyu Park, Chu-Young Cho, Clare Chisu Byeon, and Seong-Ju Park. Surface-plasmon-enhanced light-emitting diodes. *Advanced Materials*, 20(7):1253–1257, 2008.

[5] Lujun Huang, Yiling Yu, and Linyou Cao. General modal properties of optical resonances in subwavelength nonspherical dielectric structures. *Nano letters*, 13(8):3559–3565, 2013.

[6] J Van de Groep and A Polman. Designing dielectric resonators on substrates: Combining magnetic and electric resonances. *Optics express*, 21(22):26285–26302, 2013.

[7] Rebecca Sainidou, Jan Renger, Tatiana V Teperik, Mara Gonzalez, Romain Quidant, and F Javier Garcia de Abajo. Extraordinary all-dielectric light enhancement over large volumes. *Nano letters*, 10(11):4450–4455, 2010.

[8] Peter W Barber and Richard Kounai Chang. *Optical effects associated with small particles*, volume 1. World Scientific, 1988.

[9] Craig F Bohren and Donald R Huffman. *Absorption and scattering of light by small particles*. John Wiley & Sons, 2008.

[10] Gustav Mie. Beitrage zur optik truber medien, speziell kolloidaler metallosungen. *Annalen der physik*, 330(3):377–445, 1908.

[11] Jon A Schuller and Mark L Brongersma. General properties of dielectric optical antennas. *Optics express*, 17(26):24084–24095, 2009.

[12] P Spinelli, MA Verschuuren, and A Polman. Broadband omnidirectional antireflection coating based on subwavelength surface mie resonators. *Nature communications*, 3:692, 2012.

[13] Aitzol Garcia-Etxarri, R Gomez-Medina, Luis S Froufe-Perez, Cefe Lopez, L Chantada, F Scheffold, J Aizpurua, M Nieto-Vesperinas, and JJ Saenz. Strong magnetic response of submicron silicon particles in the infrared. *Optics express*, 19(6):4815–4826, 2011.

[14] Andrey B Evlyukhin, Carsten Reinhardt, Andreas Seidel, Boris S Lukyanchuk, and Boris N Chichkov. Optical response features of si-nanoparticle arrays. *Physical Review B*, 82(4):045404, 2010.

[15] Andrey B Evlyukhin, Sergey M Novikov, Urs Zywietz, Rene Lynge Eriksen, Carsten Reinhardt, Sergey I Bozhevolnyi, and Boris N Chichkov. Demonstration of magnetic dipole resonances of dielectric nanospheres in the visible region. *Nano letters*, 12(7):3749–3755, 2012.

[16] Andrey B Evlyukhin, Carsten Reinhardt, and Boris N Chichkov. Multipole light scattering by nonspherical nanoparticles in the discrete dipole approximation. *Physical Review B*, 84(23):235429, 2011.

[17] Yuan Hsing Fu, Arseniy I Kuznetsov, Andrey E Miroshnichenko, Ye Feng Yu, and Boris Luk yanchuk. Directional visible light scattering by silicon nanoparticles. *Nature communications*, 4:1527, 2013.

[18] Steven Person, Manish Jain, Zachary Lapin, Juan Jose Saenz, Gary Wicks, and Lukas Novotny. Demonstration of zero optical backscattering from single nanoparticles. *Nano letters*, 13(4):1806–1809, 2013.

[19] Isabelle Staude, Andrey E Miroshnichenko, Manuel Decker, Nche T Fofang, Sheng Liu, Edward Gonzales, Jason Dominguez, Ting Shan Luk, Dragomir N Neshev Neshev, and Igal Brener. Tailoring directional scattering through magnetic and electric resonances in subwavelength silicon nanodisks. *ACS nano*, 7(9):7824–7832, 2013.

[20] T Coenen. Angle-resolved cathodoluminescence nanoscopy. *Phd thesis, University of Amsterdam*, May 2014.

[21] Tim H Taminiau, Sinan Karaveli, Niek F van Hulst, and Rashid Zia. Quantifying the magnetic nature of light emission. *Nature communications*, 3:979, 2012.

[22] KH Drexhage, H Kuhn, and FP Schäfer. Variation of the fluorescence decay time of a molecule in front of a mirror. *Berichte der Bunsengesellschaft für physikalische Chemie*, 72(2):329–329, 1968.

[23] Arseniy I Kuznetsov, Andrey E Miroshnichenko, Yuan Hsing Fu, JingBo Zhang, and Boris Lukyanchuk. Magnetic light. *Scientific reports*, 2, 2012.

[24] Gerhard Heinrich Dieke, Henry Milton Crosswhite, and Hannah Crosswhite. Spectra and energy levels of rare earth ions in crystals. 1968.

[25] Christopher M Dodson and Rashid Zia. Magnetic dipole and electric quadrupole transitions in the trivalent lanthanide series: Calculated emission rates and oscillator strengths. *Physical Review B*, 86(12):125102, 2012.

[26] Quentin Thommen and Paul Mandel. Left-handed properties of erbium-doped crystals. *Optics letters*, 31(12):1803–1805, 2006.

[27] N Noginova, Yu Barnakov, H Li, and MA Noginov. Effect of metallic surface on electric dipole and magnetic dipole emission transitions in eu^3+ doped polymeric film. *Optics express*, 17(13):10767–10772, 2009.

[28] Martin Frimmer, Yuntian Chen, and A Femius Koenderink. Scanning emitter lifetime imaging microscopy for spontaneous emission control. *Physical review letters*, 107(12):123602, 2011.

[29] Pascal Anger, Palash Bharadwaj, and Lukas Novotny. Enhancement and quenching of single-molecule fluorescence. *Physical review letters*, 96(11):113002, 2006.

[30] personal conversation F. Rabouw. Utrecht university. 2014.

[31] FDTD Solutions. Lumerical solutions. *www.lumerical.com*, 2012.

[32] Edward D Palik. *Handbook of optical constants of solids*, volume 3. Academic press, 1998.

[33] Anke Oertel, Cornelia Lengler, Thomas Walther, and Markus Haase. Photonic properties of inverse opals fabricated from lanthanide-doped lapo4 nanocrystals. *Chemistry of Materials*, 21(16):3883–3888, 2009.

[34] Dragomir N Neshev, Isabelle Staude, Nche T Fofang, Sheng Liu, Jason Dominguez, Manuel Decker, Andrey Miroshnichenko, Vyacheslav V Khardikov, Ting S Luk, Igal Brener, et al. Shaping emission spectra of quantum dots by all-dielectric metasurfaces. In *QELS Fundamental Science*. Optical Society of America, 2014.

[35] J. F. Ziegler, M. D. Ziegler, and J. P. Biersack. Srim - the stopping and range of ions in matter (2010). *Nuclear Instruments and Methods in Physics Research B*, 268:1818–1823, June 2010.